Effect of internal mass in the lattice Boltzmann simulation of moving solid bodies by the smoothed-profile method

Yasushi Mino,[1,2,*] Hiroyuki Shinto,[3] Shohei Sakai,[1] and Hideto Matsuyama[1,†]

[1]*Center for Membrane and Film Technology, Department of Chemical Science and Engineering, Kobe University, 1-1 Rokkodai, Nada-ku, Kobe 657-8501, Japan*
[2]*Division of Applied Chemistry, Graduate School of Natural Science and Technology, Okayama University, 3-1-1 Tsushima-naka, Kita-ku, Okayama 700-8530, Japan*
[3]*Department of Chemical Engineering, Fukuoka University, 8-19-1 Nanakuma, Jonan-ku, Fukuoka 814-0180, Japan*

A computational method for the simulation of particulate flows that can efficiently treat the particle-fluid boundary in systems containing many particles was developed based on the smoothed-profile lattice Boltzmann method (SPLBM). In our proposed method, which we call the improved SPLBM (iSPLBM), for an accurate and stable simulation of particulate flows, the hydrodynamic force on a moving solid particle is exactly formulated with consideration of the effect of internal fluid mass. To validate the accuracy and stability of iSPLBM, we conducted numerical simulations of several particulate flow systems and compared our results with those of other simulations and some experiments. In addition, we performed simulations on flotation of many lightweight particles with a wide range of particle size distribution, the results of which demonstrated the effectiveness of iSPLBM. Our proposed model is a promising method to accurately and stably simulate extensive particulate flows.

I. INTRODUCTION

Particulate flows are frequently encountered in processes of various technological fields such as in industrial, environmental, and biomedical applications. Because particulate behaviors induced by flows are complicated and vary widely, their precise prediction and control are challenging. A fundamental understanding of particulate behaviors is of significant importance in technological processes. In this context, computational fluid dynamics (CFD) has been increasingly adopted as a promising approach, as it can clarify the essential mechanism of the complicated particulate flows visually and quantitatively.

The lattice Boltzmann method (LBM) [1,2] is one of the CFD techniques that is very useful for the simulation of solid-fluid multiphase flows. The LBM uses a fixed Cartesian mesh for the fluid, which is composed of Eulerian lattice nodes. It is based on the lattice Boltzmann equation, which describes the evolution of the imaginary fluid particles with a finite set of velocity vectors. The time integration for the lattice Boltzmann equation is explicit, and the collision-and-streaming procedure is conducted locally. The macroscopic fluid variables such as density, pressure, and flow velocity are calculated with the particle distribution functions at every lattice node. With the simple formulation of the LBM, its simulation can be implemented straightforwardly on parallel computer architectures. Various methods have been developed to simulate particulate flows efficiently and accurately using the LBM, some of which are briefly described below.

The most common way to treat solid-fluid boundaries within the framework of LBM is the bounce-back (BB) method [3]. The BBLBM uses a collection of boundary nodes for representing the solid surface, each of which is set at the midpoint of the link between two fixed lattice nodes of the

solid side and fluid side. Every imaginary fluid particle moving from a fluid-side node to a solid-side node is reflected at the boundary node. The time variations of these particle distribution functions are used to compute the momentum transfer at the solid-fluid interface and the resultant hydrodynamic force on the solid body. Generally, the boundary nodes move in a stepwise manner during the course of simulation, which leads to fluctuation of solid-fluid interaction. To reduce this fluctuation and improve computational accuracy, several interpolation schemes have been proposed [4,5].

The immersed-boundary (IB) method, which was originally implemented on a direct numerical simulation (DNS) solver [6], has been increasingly developed and employed for the LBM solver. The IB method uses a set of Lagrangian boundary points fixed on the surface of a solid body. The basic idea of the IB method is to treat the solid-fluid boundary as a deformable one with high stiffness. A small distortion of the boundary yields a force that restores the deformed boundary to its original shape. The restoring force is calculated at every boundary point and then distributed to the lattice node(s) near the boundary to enforce the no-slip condition on the solid-fluid boundary, where interpolation is performed between the Eulerian fluid-side lattice nodes and the Lagrangian boundary points. Calculations for the restoring force are classified into three main approaches, namely, the penalty method [7], direct forcing method [8,9], and momentum exchange method [10].

An alternative promising method to treat the particle-fluid boundary is the smoothed-profile (SP) method [11,12], which is based on the diffuse-interface model and can be interpreted as a variation of the IB method [13]. The SP method was proposed for a DNS solver by Nakayama and Yamamoto [11] and then developed for an LBM solver (SPLBM) by Jafari *et al.* [12]. In the SP method, the original sharp interface between the particle and the host fluid is replaced by a smoothed interface with a finite thickness. Because of the introduction of this smoothed interface, the momentum exchanges in the SP method are conducted at the fixed Eulerian

---
*ymino@okayama-u.ac.jp
†matuyama@kobe-u.ac.jp

lattice nodes, instead of at the movable Lagrangian boundary points on the solid surface used in the original IB method. Thus the SP method eliminates the complex interpolation procedures between the fixed lattice nodes and the movable boundary points, which is a great advantage particularly for the simulation of systems containing many particles. However, smoothed-profile CFD simulations suffer from computational inaccuracy and instability and are consequently restricted to particulate flows at low Reynolds numbers; for example, Hashemi *et al.* [14] demonstrated that the SPLBM estimates the hydrodynamic force on a single sedimenting particle less accurately with increasing Reynolds number. This problem should be addressed for accurate and stable smoothed-profile CFD simulations of various particulate flows.

In the present study, we propose the improved SPLBM (iSPLBM) for an accurate and stable simulation of particulate flows, where the hydrodynamic force on a moving solid particle is exactly formulated with consideration of the effect of internal fluid mass that was neglected in the original SP method [11,12]. To validate the accuracy and stability of our iSPLBM, we carried out numerical simulations of several particulate flow systems and compared our results with those of other simulations and some experiments. Finally, we demonstrate the effectiveness of our iSPLBM by performing simulations of flotation of many lightweight particles with a wide range of particle size distribution, which is one of the challenging systems in CFD simulations.

II. NUMERICAL MODELING

We consider a system where N_p rigid particles of circular [two-dimensional (2D)] or spherical [three-dimensional (3D)] shapes are dispersed in an incompressible Newtonian fluid. In the SP method, the original sharp interfaces between the solid particles and host fluid are replaced by smoothed interfaces with a finite thickness ξ [11]. With reference to Fig. 1, let Ω^all be the entire domain of the system, while $\Gamma_k(t)$ and $\Omega_k^\mathrm{in}(t)$ are, respectively, the original surface and the internal domain of the kth particle with radius a_k ($k = 1, 2, \ldots, N_\mathrm{p}$) at time t, where $\Omega_k^\xi(t)$ represents the smoothed-interface domain of the kth particle. It is noted that only the inner part of $\Omega_k^\xi(t)$ cut by $\Gamma_k(t)$ is involved in $\Omega_k^\mathrm{in}(t)$, whereas the outer part of $\Omega_k^\xi(t)$ stays outside of $\Omega_k^\mathrm{in}(t)$.
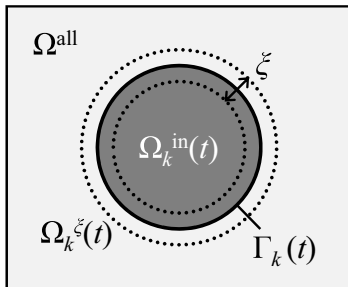

FIG. 1. Schematic illustration of the kth rigid particle suspended in an incompressible and Newtonian fluid. In the smoothed-profile (SP) method, the original sharp interface between the particle and host fluid is replaced by a smoothed interface with a finite thickness ξ

A. Fluid flow with solid particles described by SP method

The SP method assumes that the internal and interface domains, $\Omega^\mathrm{in}(t)$ and $\Omega^\xi(t)$, respectively, are filled with an artificial fluid of the same physical properties (i.e., density and viscosity) as the host fluid. The motion of this fluid flow is governed by the continuity equation and the Navier-Stokes equation:

$$\nabla \cdot \boldsymbol{u} = 0, \tag{1}$$

$$\frac{\partial \boldsymbol{u}}{\partial t} + (\boldsymbol{u} \cdot \nabla)\boldsymbol{u} = -\frac{1}{\rho_\mathrm{f}}\nabla p + \nu_\mathrm{f}\nabla^2 \boldsymbol{u} + \phi \boldsymbol{f}_\mathrm{p}, \tag{2}$$

where $\boldsymbol{u}$ is the fluid velocity, ρ_f is the fluid density, p is the pressure, and ν_f is the fluid kinematic viscosity. The term $\phi \boldsymbol{f}_\mathrm{p}$ in Eq. (2) is the body force to enforce the particle rigidity and the no-slip condition on the particle surface. The exact formulation of this body force is given in Sec. II C.

B. Motion of particles

The translational and rotational motions of the kth particle with circular or spherical shape are expressed by the Newton-Euler equations:

$$\frac{\mathrm{d}\boldsymbol{X}_k}{\mathrm{d}t} = \boldsymbol{V}_k, \tag{3}$$

$$M_k\frac{\mathrm{d}\boldsymbol{V}_k}{\mathrm{d}t} = \boldsymbol{F}_k^\mathrm{H} + \boldsymbol{F}_k^\mathrm{P} + \boldsymbol{F}_k^\mathrm{G}, \tag{4}$$

$$\boldsymbol{I}_k \cdot \frac{\mathrm{d}\boldsymbol{\Omega}_k}{\mathrm{d}t} = \boldsymbol{N}_k^\mathrm{H}, \tag{5}$$

where $\boldsymbol{X}_k$, $\boldsymbol{V}_k$, $\boldsymbol{\Omega}_k$, M_k, and $\boldsymbol{I}_k$ are the center-of-mass position, translational velocity, angular velocity, mass, and inertial tensor of the kth particle, respectively. $\boldsymbol{F}_k^\mathrm{H}$ and $\boldsymbol{N}_k^\mathrm{H}$ are the hydrodynamic force and torque, respectively, as formulated in Sec. II C. The term $\boldsymbol{F}_k^\mathrm{P}$ is the force arising from the excluded volume of particles that prevents the particles from overlapping with each other and with the solid walls. In the present study, $\boldsymbol{F}_k^\mathrm{P}$ is represented by the repulsive part of the Lennard-Jones potential for particle-particle and particle-wall direct interactions [11] for the sake of simplicity. $\boldsymbol{F}_k^\mathrm{G}$ is a set of gravitational and buoyant forces; $\boldsymbol{F}_k^\mathrm{G} = M_k(1 - \rho_\mathrm{f}/\rho_\mathrm{p})\boldsymbol{a}_\mathrm{g}$, where ρ_p is the mass density of the particles and $\boldsymbol{a}_g$ is the gravitational acceleration.

C. Improved smoothed-profile method

The existence of N_p particles is expressed as a continuous field over the computational domain:

$$\phi(\boldsymbol{x}, t) = \sum_{k=1}^{N_\mathrm{p}} \phi_k(\boldsymbol{x}, t), \tag{6}$$

where $\phi_i(\boldsymbol{x}, t)$ is the smoothed-profile function for the kth particle ($k = 1, 2, \ldots, N_\mathrm{p}$) at a fixed Eulerian lattice node $\boldsymbol{x}$ and time t. The spatial profile of ϕ_k is defined such that the values of $\phi_k = 1$ and $\phi_k = 0$ represent the particle-side and fluid-side domains outside of $\Omega_k^\xi(t)$, respectively, and ϕ_k continuously changes between these two values within the interfacial domain $\Omega_k^\xi(t)$. A specific form should be selected

for the smoothed profile, according to the physical modeling of the system under consideration. Three typical forms of the smoothed profile are given in Ref. [11]. Throughout the present study, we employed the smoothed profile given by

$$\phi_k(\boldsymbol{x}) = s(a_k - |\boldsymbol{x} - \boldsymbol{X}_k|),$$

$$s(x) = \begin{cases} 0, & x < -\xi/2, \\ \frac{1}{2}\big[\sin\big(\frac{\pi x}{\xi}\big) + 1\big], & |x| \leqslant \xi/2, \\ 1, & x > \xi/2. \end{cases} \quad (7)$$

The particle velocity field $\boldsymbol{u}_\mathrm{p}(\boldsymbol{x},t)$ is defined using $\{\boldsymbol{X}_k, \boldsymbol{V}_k, \boldsymbol{\Omega}_k, \phi_k\}$ as

$$\phi(\boldsymbol{x},t)\boldsymbol{u}_\mathrm{p}(\boldsymbol{x},t) = \sum_{k=1}^{N_\mathrm{p}} \phi_k(\boldsymbol{x},t)[\boldsymbol{V}_k(t) + \boldsymbol{\Omega}_k(t) \times \{\boldsymbol{x} - \boldsymbol{X}_k(t)\}].$$

(8)

The total (fluid+particle) velocity field $\boldsymbol{u}(\boldsymbol{x},t)$ is then expressed by

$$\boldsymbol{u}(\boldsymbol{x},t) = (1 - \phi)\boldsymbol{u}_\mathrm{f} + \phi\boldsymbol{u}_\mathrm{p} = \boldsymbol{u}_\mathrm{f} + \phi(\boldsymbol{u}_\mathrm{p} - \boldsymbol{u}_\mathrm{f}). \quad (9)$$

To derive the evolution of the total velocity $\boldsymbol{u}$, the fluid velocity $\boldsymbol{u}_\mathrm{f}$ is solved. By integrating Eq. (2) without the body force term $\phi\boldsymbol{f}_\mathrm{p}$, the total velocity is predicted as $\boldsymbol{u} = \boldsymbol{u}^*$ with the pressure that satisfies the incompressibility condition $\nabla \cdot \boldsymbol{u}^* = 0$. To enforce Eq. (9) and the solid-fluid impermeability condition, the time-integrated body force $\phi\boldsymbol{f}_\mathrm{p}$ is determined as

$$\int_t^{t+\Delta t} \phi\boldsymbol{f}_\mathrm{p}\mathrm{d}t' = \phi(\boldsymbol{x},t+\Delta t)[\boldsymbol{u}_\mathrm{p}(\boldsymbol{x},t+\Delta t)$$
$$- \boldsymbol{u}^*(\boldsymbol{x},t+\Delta t)] - \frac{\Delta t}{\rho_\mathrm{f}}\nabla p_\mathrm{p}, \quad (10)$$

where the pressure p_p is determined to satisfy $\nabla \cdot \boldsymbol{u} = (\nabla\phi) \cdot (\boldsymbol{u}_\mathrm{p} - \boldsymbol{u}^*) = 0$. By correcting $\boldsymbol{u}^*$ with the body force, the total velocity field $\boldsymbol{u}(\boldsymbol{x},t+\Delta t)$ is obtained. As for the LBM solver, this algorithm is reduced to a simple explicit form without solving any Poisson equation, as will be given using Eqs. (23) and (24) in Sec. III A, where negligible errors are caused by the compressibility effect that is inherent in the LBM.

The hydrodynamic force $\boldsymbol{F}_k^\mathrm{H}(t)$ acting on the kth particle at time t is calculated based on the momentum exchange between the particle and fluid during the time interval Δt. In the original SP method, the hydrodynamic force is simply expressed as the volume integral of the body force over the kth particle volume:

$$\boldsymbol{F}_k^\mathrm{H,tot}(t) = -\int_{\boldsymbol{x}\in[\Omega_k^\mathrm{in}\cup\Omega_k^\xi]} \rho_\mathrm{f}\phi_k\boldsymbol{f}_\mathrm{p}(\boldsymbol{x},t)\mathrm{d}\boldsymbol{x}. \quad (11)$$

It should be noted that $\boldsymbol{F}_k^\mathrm{H,tot}(t)$ is not exactly the actual hydrodynamic force $\boldsymbol{F}_k^\mathrm{H}(t)$, because $\boldsymbol{F}_k^\mathrm{H,tot}(t)$ contains the force that compels the velocity of the artificial fluid inside the kth particle to be consistent with the translational and rotational velocities of the particle. For calculation of the actual hydrodynamic force $\boldsymbol{F}_k^\mathrm{H}(t)$, $\boldsymbol{F}_k^\mathrm{H,tot}(t)$ given by Eq. (11) must be compensated with the force to move the artificial fluid of $\Omega_k^\mathrm{in}(t)$. This compensation force $\boldsymbol{F}_k^\mathrm{H,in}(t)$ is given by the time derivative of the linear momentum of the artificial

fluid of $\Omega_k^\mathrm{in}(t)$:

$$\boldsymbol{F}_k^\mathrm{H,in}(t) = \frac{\mathrm{d}}{\mathrm{d}t}\int_{\boldsymbol{x}\in\Omega_k^\mathrm{in}} \rho_\mathrm{f}\boldsymbol{u}(\boldsymbol{x},t)\mathrm{d}\boldsymbol{x}. \quad (12)$$

Since the artificial fluid inside every particle is enforced to move as a rigid body in the SP method, Eq. (12) should read

$$\boldsymbol{F}_k^\mathrm{H,in}(t) = \rho_\mathrm{f}\frac{\mathrm{d}}{\mathrm{d}t}\int_{\boldsymbol{x}\in\Omega_k^\mathrm{in}} [\boldsymbol{V}_k(t) + \boldsymbol{\Omega}_k(t) \times \{\boldsymbol{x} - \boldsymbol{X}_k(t)\}]\mathrm{d}\boldsymbol{x}$$
$$= \rho_\mathrm{f}\frac{\mathrm{d}\boldsymbol{V}_k(t)}{\mathrm{d}t}\int_{\boldsymbol{x}\in\Omega_k^\mathrm{in}} \mathrm{d}\boldsymbol{x} = \frac{\rho_\mathrm{f}}{\rho_\mathrm{p}}M_k\frac{\mathrm{d}\boldsymbol{V}_k(t)}{\mathrm{d}t}, \quad (13)$$

which is expressed by the time derivative of the linear momentum of the rigid body having the same volume as that of the particle (M_k/ρ_p) and the same mass density as that of the host fluid (ρ_f). Consequently, $\boldsymbol{F}_k^\mathrm{H}(t)$ is calculated by

$$\boldsymbol{F}_k^\mathrm{H}(t) = \boldsymbol{F}_k^\mathrm{H,tot}(t) + \boldsymbol{F}_k^\mathrm{H,in}(t). \quad (14)$$

In a similar way, the hydrodynamic torque $\boldsymbol{N}_k^\mathrm{H}(t)$ acting on the kth particle at time t is calculated as follows:

$$\boldsymbol{N}_k^\mathrm{H}(t) = \boldsymbol{N}_k^\mathrm{H,tot}(t) + \boldsymbol{N}_k^\mathrm{H,in}(t), \quad (15)$$

$$\boldsymbol{N}_k^\mathrm{H,tot}(t) = -\int_{\boldsymbol{x}\in[\Omega_k^\mathrm{in}\cup\Omega_k^\xi]} \rho_\mathrm{f}[\boldsymbol{x} - \boldsymbol{X}_k(t)] \times \phi_k\boldsymbol{f}_\mathrm{p}(\boldsymbol{x},t)\mathrm{d}\boldsymbol{x}, \quad (16)$$

$$\boldsymbol{N}_k^\mathrm{H,in}(t) = \frac{\mathrm{d}}{\mathrm{d}t}\int_{\boldsymbol{x}\in\Omega_k^\mathrm{in}} \rho_\mathrm{f}[\boldsymbol{x} - \boldsymbol{X}_k(t)] \times \boldsymbol{u}(\boldsymbol{x},t)\mathrm{d}\boldsymbol{x}$$
$$= \rho_\mathrm{f}\frac{\mathrm{d}}{\mathrm{d}t}\int_{\boldsymbol{x}\in\Omega_k^\mathrm{in}} [\boldsymbol{x} - \boldsymbol{X}_k(t)]$$
$$\times [\boldsymbol{V}_k(t) + \boldsymbol{\Omega}_k(t) \times \{\boldsymbol{x} - \boldsymbol{X}_k(t)\}]\mathrm{d}\boldsymbol{x}$$
$$= \rho_\mathrm{f}\frac{\mathrm{d}}{\mathrm{d}t}\int_{\boldsymbol{x}\in\Omega_k^\mathrm{in}} [\boldsymbol{x} - \boldsymbol{X}_k(t)] \times \boldsymbol{\Omega}_k(t) \times [\boldsymbol{x} - \boldsymbol{X}_k(t)]\mathrm{d}\boldsymbol{x}$$
$$= \frac{\rho_\mathrm{f}}{\rho_\mathrm{p}}\boldsymbol{I}_k \cdot \frac{\mathrm{d}\boldsymbol{\Omega}_k(t)}{\mathrm{d}t}. \quad (17)$$

Hereafter, the compensation force $\boldsymbol{F}_k^\mathrm{H,in}(t)$ and torque $\boldsymbol{T}_k^\mathrm{H,in}(t)$ are called the internal mass effect, which is neglected in the original SP method [11,12]. The same expressions of hydrodynamic force and torque on a moving particle, Eqs. (14) and (15), have been employed in the IB method with several direct forcing approaches, where different schemes for computing the internal mass effect were proposed [15–19]. Feng and Michaelides [17] developed a successful IB–direct-forcing scheme on the basis of Eqs. (13) and (17). Thus the IB method of Feng and Michaelides [17] and our iSP method rely on the same idea, but are distinct from each other in details; especially, the former uses a set of Lagrangian boundary points fixed on the surface of a solid body, whereas the latter replaces the original sharp interface between the particle and the fluid by a smoothed interface with a finite thickness.

III. NUMERICAL METHOD

A. Lattice Boltzmann method

The fluid motion is solved using the LBM [20] in the present model. The nondimensional variables used henceforth are

defined by a characteristic length $\hat{H}_0$, a characteristic particle speed $\hat{c}$, a characteristic time scale $\hat{t}_0 = \hat{H}_0/\hat{U}_0$, where $\hat{U}_0$ is a characteristic flow speed, and a reference fluid density $\hat{\rho}_f$. It should be noted that the relation between the nondimensional time step Δt and the nondimensional lattice spacing Δx is given by $\Delta t = \mathrm{Sh}\Delta x$, where $\mathrm{Sh} = \hat{H}_0/(\hat{t}_0\hat{c}) = \hat{U}_0/\hat{c}$. In the LBM, a modeled fluid, composed of imaginary fluid particles with a finite set of vectors, is considered. We used the two-dimensional nine-velocity (D2Q9) model and three-dimensional 15-velocity (D3Q15) model. The physical space is divided into a square lattice and a cubic lattice for the D2Q9 model and the D3Q15 model, respectively. The D2Q9 model has velocity vectors $c_i = (0,0)$, $(0,\pm 1)$, $(\pm 1,0)$, and $(\pm 1,\pm 1)$ for $i = 1,2,\ldots,9$. The D3Q15 model has velocity vectors $c_i = (0,0,0)$, $(0,0,\pm 1)$, $(0,\pm 1,0)$, $(\pm 1,0,0)$, and $(\pm 1,\pm 1,\pm 1)$ for $i = 1,2,\ldots,15$.

The evolution of the particle distribution function $f_i(x,t)$ with velocity c_i at lattice point x and time t is computed by the following equation:

$$f_i(x + c_i\Delta x, t + \Delta t) = f_i(x,t) - \frac{1}{\tau}\big[f_i(x,t) - f_i^{\mathrm{eq}}(x,t)\big],$$
(18)

where Δx is the lattice spacing, Δt is the time step during which the fluid particles travel one lattice spacing, f_i^{eq} is an equilibrium distribution function, and τ is the relaxation time. For incompressible fluid flows, f_i^{eq} is given by

$$f_i^{\mathrm{eq}} = E_i\big[3p + 3c_i \cdot u + \tfrac{9}{2}(c_i \cdot u)^2 - \tfrac{3}{2}u \cdot u\big],$$
(19)

where $E_1 = 4/9$, $E_2 = \cdots = E_5 = 1/9$, and $E_6 = \cdots = E_9 = 1/36$ for the D2Q9 model, and $E_1 = 2/9$, $E_2 = \cdots = E_7 = 1/9$, and $E_8 = \cdots = E_{15} = 1/72$ for the D3Q15 model [21]. The pressure $p(x,t)$ and the flow velocity $u(x,t)$ are calculated with the particle distribution functions as follows:

$$p(x,t) = \frac{1}{3}\sum_{i=1}^{b} f_i(x,t),$$
(20)

$$u(x,t) = \sum_{i=1}^{b} f_i(x,t)c_i,$$
(21)

where $b = 9$ for the D2Q9 model and $b = 15$ for the D3Q15 model. The kinematic viscosity ν_f is given by the following relation:

$$\nu_f = \tfrac{1}{3}\big(\tau - \tfrac{1}{2}\big)\Delta x.$$
(22)

When an external body force $g(x,t)$ is applied, the evolution equation of the particle distribution function $f_i(x,t)$ can be calculated by a fractional step approach [20]:

(i) The intermediate value of f_i without the body force, f_i^*, is calculated by

$$f_i^*(x + c_i\Delta x, t + \Delta t) = f_i(x,t) - \frac{1}{\tau}\big[f_i(x,t) - f_i^{\mathrm{eq}}(x,t)\big].$$
(23)

(ii) $f_i(x,t + \Delta t)$ is obtained by correcting $f_i^*(x,t + \Delta t)$ with the body force:

$$f_i(x,t + \Delta t) = f_i^*(x,t + \Delta t) + 3\Delta x E_i c_i \cdot g(x,t + \Delta t).$$
(24)

B. Computational procedure

At the initial step ($t = 0$), $X_k(0)$, $V_k(0)$, $\Omega_k(0)$, $u(x,0)$, and $p(x,0)$ are assigned, and $f_i(x,0)$ is assumed to be f_i^{eq} with $u(x,0)$ and $p(x,0)$, whereas $F_k^{\mathrm{H}}(0)$ and $N_k^{\mathrm{H}}(0)$ are assumed to be zero. It is supposed that $X_k(t)$, $V_k(t)$, $\Omega_k(t)$, $f_i(x,t)$, $u(x,t)$, and $p(x,t)$ are known immediately before the computation at time $t + \Delta t$. The computation procedure is given below.

(i) Using the forces and torques obtained at time t, $V_k(t + \Delta t)$ and $\Omega_k(t + \Delta t)$ are calculated using Eqs. (4) and (5) with the first-order Euler explicit scheme as

$$V_k(t + \Delta t) = V_k(t) + \frac{\Delta t}{\mathrm{Sh}}M_k^{-1}\big[F_k^{\mathrm{H}}(t) + F_k^{\mathrm{P}}(t) + F_k^{\mathrm{G}}(t)\big],$$
(25)

$$\Omega_k(t + \Delta t) = \Omega_k(t) + \frac{\Delta t}{\mathrm{Sh}}I_k^{-1} \cdot N_k^{\mathrm{H}}(t).$$
(26)

$X_k(t + \Delta t)$ is then updated using Eq. (3) with the Crank-Nicolson scheme as

$$X_k(t + \Delta t) = X_k(t) + \frac{\Delta t}{2\mathrm{Sh}}[V_k(t) + V_k(t + \Delta t)].$$
(27)

(ii) $\phi(x,t + \Delta t)$ and $u_{\mathrm{p}}(x,t + \Delta t)$ are calculated using Eqs. (6)–(8) with $V_k(t + \Delta t)$, $\Omega_k(t + \Delta t)$, and $X_k(t + \Delta t)$.

(iii) After calculating $f_i^*(x,t + \Delta t)$ using Eq. (23), $u^*(x,t + \Delta t)$ is calculated using Eq. (21) as

$$u^*(x,t + \Delta t) = \sum_{i=1}^{b} f_i^*(x,t + \Delta t)c_i.$$
(28)

ϕf_{p} is calculated using Eq. (10) as

$$\phi f_{\mathrm{p}}(x,t + \Delta t) = \phi(x,t + \Delta t)\frac{\mathrm{Sh}}{\Delta t}[u_{\mathrm{p}}(x,t + \Delta t) - u^*(x,t + \Delta t)].$$
(29)

(iv) $f_i(x,t + \Delta t)$ is calculated using Eq. (24) as

$$f_i(x,t + \Delta t) = f_i^*(x,t + \Delta t) + 3\Delta x E_i c_i \cdot \phi f_{\mathrm{p}}(x,t + \Delta t).$$
(30)

$p(x,t + \Delta t)$ and $u(x, t + \Delta t)$ are calculated using Eqs. (20) and (21) with Eq. (30). Note that $u(x, t + \Delta t)$ satisfies the no-slip boundary condition on the particle-fluid interfaces, because $\phi f_{\mathrm{p}}(x,t + \Delta t)$ has been determined using $u^*(x,t + \Delta t)$.

(v) $F_k^{\mathrm{H,tot}}(t + \Delta t)$ and $N_k^{\mathrm{H,tot}}(t + \Delta t)$ are calculated using Eqs. (11) and (16) with Eq. (29):

$$F_k^{\mathrm{H,tot}}(t + \Delta t) = -\frac{\mathrm{Sh}}{\Delta t}\rho_f \sum_{x\in\Omega^{\mathrm{all}}} \phi_k(x,t + \Delta t) \times f_{\mathrm{p}}(x,t + \Delta t)(\Delta x)^d,$$
(31)

$$N_k^{\mathrm{H,tot}}(t + \Delta t) = -\frac{\mathrm{Sh}}{\Delta t}\rho_f \sum_{x\in\Omega^{\mathrm{all}}} \phi_k(x,t + \Delta t)[x - X_k(t + \Delta t)] \times f_{\mathrm{p}}(x,t + \Delta t)(\Delta x)^d,$$
(32)

where d represents the dimensionality. On the other hand, $\boldsymbol{F}_k^{\mathrm{H,in}}$ and $\boldsymbol{N}_k^{\mathrm{H,in}}$ are, respectively, calculated using Eqs. (13) and (17) as

$$\boldsymbol{F}_k^{\mathrm{H,in}}(t + \Delta t) = \frac{\mathrm{Sh}}{\Delta t}\frac{\rho_{\mathrm{f}}}{\rho_{\mathrm{p}}}M_k[\boldsymbol{V}_k(t + \Delta t) - \boldsymbol{V}_k(t)], \quad (33)$$

$$\boldsymbol{N}_k^{\mathrm{H,in}}(t + \Delta t) = \frac{\mathrm{Sh}}{\Delta t}\frac{\rho_{\mathrm{f}}}{\rho_{\mathrm{p}}}\boldsymbol{I}_k \cdot [\boldsymbol{\Omega}_k(t + \Delta t) - \boldsymbol{\Omega}_k(t)]. \quad (34)$$

As a result, $\boldsymbol{F}_k^{\mathrm{H}}(t + \Delta t)$ and $\boldsymbol{N}_k^{\mathrm{H}}(t + \Delta t)$ are calculated using Eqs. (14) and (15), respectively.

IV. RESULTS AND DISCUSSION

A. Flow past a stationary circular cylinder

We first considered the flow past a stationary circular cylinder, which had a diameter of $D = 20\Delta x$ and an interface thickness of $\xi = \Delta x$ or $2\Delta x$, and was fixed at the center of the computational domain of $800\Delta x \times 800\Delta x$. The uniform flow of speed U_∞ came along the x axis from the left boundary and continuously went out to the right boundary, whereas the top and bottom boundaries were slip walls. The Reynolds number for this system is defined as $\mathrm{Re} = U_\infty D/\nu_{\mathrm{f}}$, where $\nu_{\mathrm{f}} = 0.05\Delta x$ and $0.025\Delta x$ (i.e., $\tau = 0.65$ and 0.575) were used.

Figure 2 displays the streamlines of steady flow at $\mathrm{Re} = 20$ and 40 for $\xi = \Delta x$. Once the flows reach the steady state, a pair of stationary recirculating eddies with x length, L, is developed behind the cylinder at every value of Re. The length of the recirculating eddy increases with Re. It should be noted that no stream lines penetrated into the solid body.

The drag coefficient, $C_{\mathrm{D}} = F_x^{\mathrm{H}}/(0.5\rho_f U_\infty^2 D)$, and the nondimensional length of the recirculation region, $L_{\mathrm{w}} = 2L/D$, were estimated for four systems with different values of ξ and Re, as summarized in Table I, where the simulation results of other methods [9,10,12,22] are also given for comparison. The results of our iSPLBM agree well with those of other methods. Although the value of L_{w} is slightly larger than those of other methods, this overestimation was reduced using a smaller interface thickness of ξ. These results indicate that the overestimation of the recirculation eddies in iSPLBM is mainly attributed to the diffuse interface between the solid and fluid, and that the smaller interface thickness is more preferable; however, the diffuse solid-fluid interface should be sufficiently thick to guarantee the accurate calculation of moving solid bodies [11]. Henceforth, $\xi = \Delta x$ was employed in further simulations.

B. Translationally oscillating circular cylinder in a stationary fluid

Let us consider the two-dimensional fluid motion induced by the translational oscillation of a circular cylinder. This phenomenon was investigated both experimentally and numerically by Dütsch et al. [23] and has been scrutinized to validate the numerical models in many studies [19,24]. A circular cylinder with a diameter of $D = 50\Delta x$ was initially located at the center of the computational domain of $1500\Delta x \times 1000\Delta x (= 30D \times 20D)$, where the Neumann condition was applied to all boundaries of the domain. The
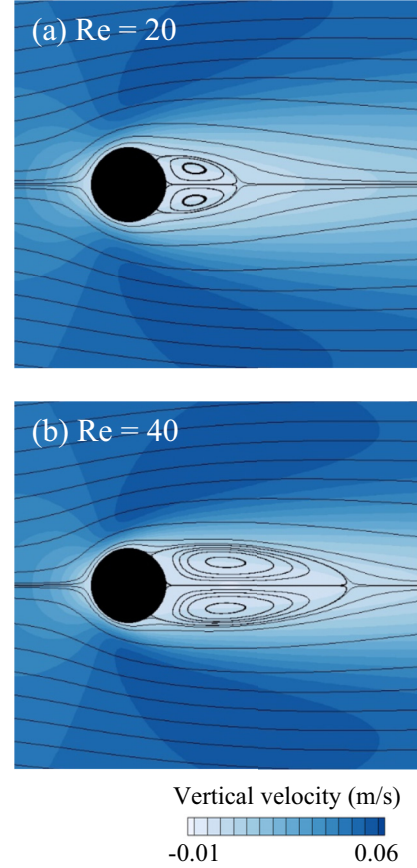

FIG. 2. Streamlines of steady flow past a stationary circular cylinder, which had a diameter of $D = 20\Delta x$ and an interface thickness of $\xi = \Delta x$, and was fixed at the center of the computational domain of $800\Delta x \times 800\Delta x$: (a) $\mathrm{Re} = 20$ and (b) $\mathrm{Re} = 40$. The flows of $|\boldsymbol{u}| < 10^{-15}$ are not shown for visual clarity.

cylinder was oscillated with the speed given as

$$U_{\mathrm{C}}(t) = -U_{\max}\cos\left(\frac{2\pi}{T}t\right), \quad (35)$$

$$V_{\mathrm{C}}(t) = 0, \quad (36)$$

where $U_{\mathrm{C}}(t)$ and $V_{\mathrm{C}}(t)$ are the velocity components of the cylinder in the x and y directions, respectively. As

TABLE I. The drag coefficient, $C_{\mathrm{D}} = F_x^{\mathrm{H}}/(0.5\rho_f U_\infty^2 D)$, and the nondimensional length of the recirculation region, $L_{\mathrm{w}} = 2L/D$, for the flow past a stationary circular cylinder, estimated using various methods.

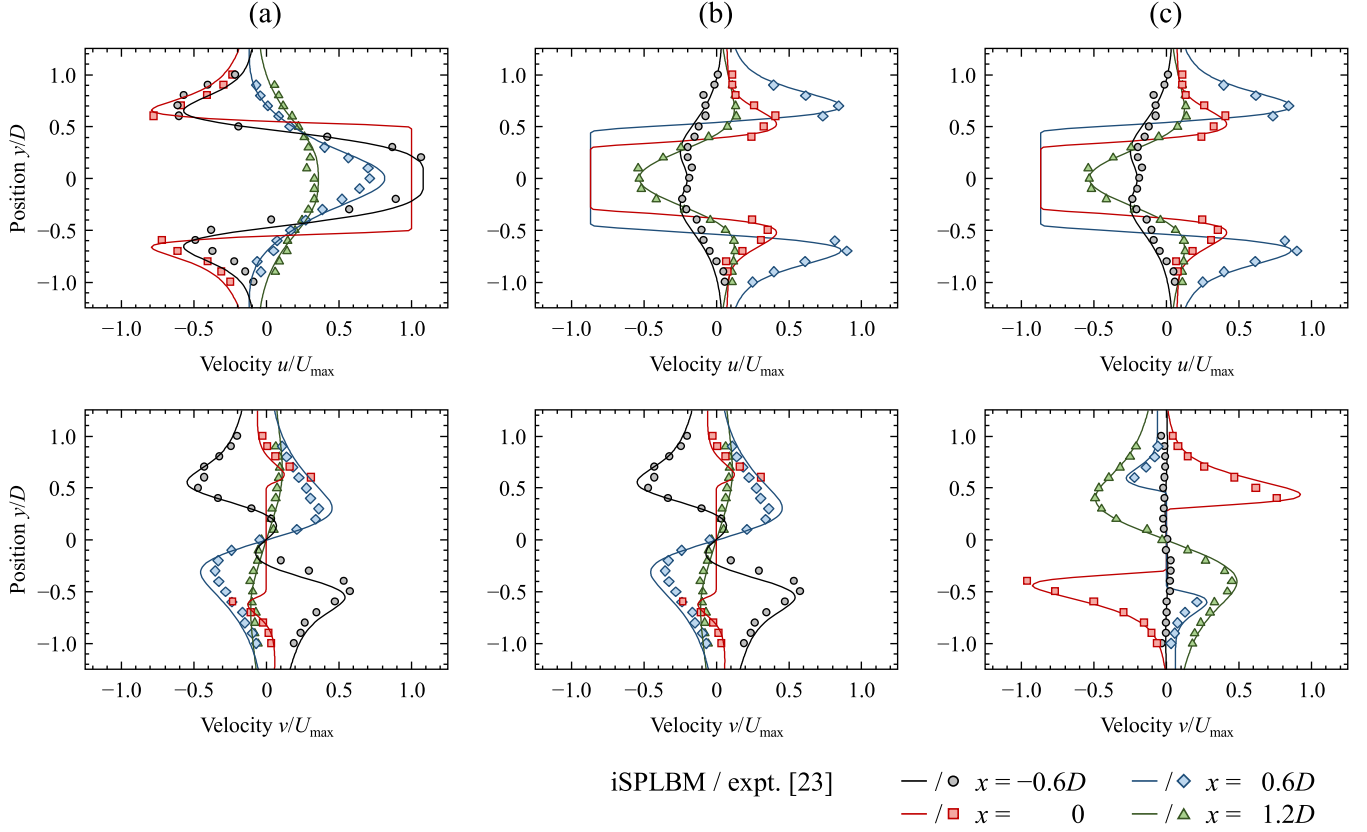| Reference	Method	Re = 20		Re = 40	
		C_{D}	L_{W}	C_{D}	L_{W}
Present study ($\xi = \Delta x$)	iSPLBM	2.080	1.94	1.572	4.94
Present study ($\xi = 2\Delta x$)	iSPLBM	2.102	2.04	1.590	5.11
Dennis and Chang [22]	FDM	2.045	1.88	1.522	4.69
Niu et al. [10]	BBLBM	2.144	1.89	1.589	4.52
Wu and Shu [9]	IBLBM	2.091	1.86	1.565	4.62
Jafari et al. [12]	SPLBM	2.112	1.914	1.598	4.81

FIG. 3. Velocity profiles of the two-dimensional fluid motion induced by the translationally oscillating circular cylinder for the case of Re = 100 and KC = 5. The velocity profiles are at the four different x positions, $x = -0.6D$, 0, 0.6D, and 1.2D, for three different phase angles $t/T =$(a) $n + 1/2$, (b) $n + 7/12$, and (c) $n + 11/12$, where n is an integer number. The results of improved smoothed-profile lattice Boltzmann method (iSPLBM) are compared with experimental results by Dütsch *et al.* [23].

for the oscillatory velocity of $U_C(t)$, U_{max} and T are the amplitude and the time period of the oscillation, respectively. The governing parameters of the system are the Reynolds number, Re = $U_{max}D/\nu_f$, and the Keulegan-Carpenter number, KC = $U_{max}T/D$. The parameter sets for the present simulations are Re = 1, 10, and 100 with KC = 5, where $\nu_f = 0.25\Delta x$, $0.10\Delta x$, and $0.025\Delta x$ (i.e., $\tau = 1.25$, 0.8, and 0.575) were used.

The velocity profiles for the case of Re = 100 are displayed in Fig. 3, where the experimental results by Dütsch *et al.* [23] are also shown for comparison. It is demonstrated that the results of our iSPLBM are in good agreement with the experimental results. The time variation of the drag coefficient defined as $C_D = 2F_x^H/(U_{max}^2 D)$ is shown in Fig. 4(a), where the simulation results are depicted after the initial transient period (i.e., $t/T \geqslant 1$). In order to confirm the validity of our iSPLBM, the results using the conventional SPLBM, in which F^H was approximated by $F^{H,tot}$ (see Sec. II C), are also shown in Fig. 4(a). A comparison suggests that the simulation result of iSPLBM is consistent with that of DNS by Dütsch *et al.* [23], whereas SPLBM overestimates the hydrodynamic force acting on the oscillating cylinder. Thus SPLBM is not capable of eliminating the extra force that drives the artificial fluid inside a moving particle; however, this can be done using iSPLBM when computing the hydrodynamic forces on the particle.

The time variations of C_D for Re = 10 and 1 are shown in Figs. 4(b) and 4(c), respectively. A comparison among the results for Re = 1, 10, and 100 indicates that the conventional SPLBM overestimates the time variations of C_D and this overestimation decreases with decreasing Re. This is because the oscillating cylinder for the smaller values of Re has smaller magnitudes of its acceleration, which induces the smaller extra force acting on the artificial fluid in itself. The difference in simulation results of moving solid particles between iSPLBM and SPLBM should be negligible for Re < 1, where the forces acting on the solid-side artificial fluid are negligibly small.

C. Sedimentation of a single sphere

Here, we consider a spherical particle sedimenting under gravity in a closed box. This phenomenon was experimentally investigated by ten Cate *et al.* [15] and has been examined to validate the numerical models in many studies [14,15,17,19,24]. Hashemi *et al.* [14] demonstrated that SPLBM estimates the hydrodynamic force on a single sedimenting sphere less accurately than BBLBM at higher Reynolds numbers. The poor accuracy of SPLBM is attributable to the neglect of the forces acting on the solid-side artificial fluid, as described in Sec. IV B.

We performed three-dimensional simulations of a sedimenting sphere using iSPLBM as well as SPLBM, and
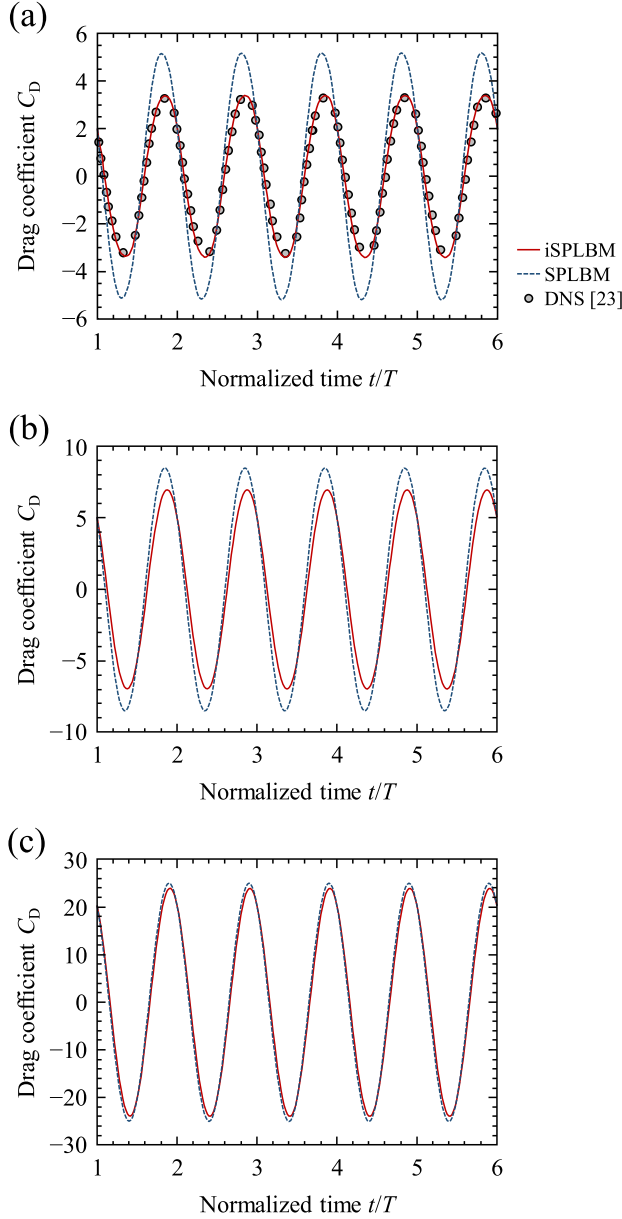
(a)

(b)

(c)

FIG. 4. Time variation of the drag coefficient C_D of a translationally oscillating circular cylinder: (a) Re = 100 and KC = 5; (b) Re = 10 and KC = 5; (c) Re = 1 and KC = 5. The results of iSPLBM are compared with those of the smoothed-profile lattice Boltzmann method (SPLBM) and experimental results by Dütsch *et al.* [23] in graph (a) and the results of SPLBM in graphs (b,c).

compared the simulation results with the experimental results by ten Cate *et al.* [15]. The experimental conditions reported therein are summarized in Table II. The closed box had dimensions of $100 \times 100 \times 160$ mm and was filled with fluid of mass density $\hat{\rho}_f$ ranging from 960 to 970 kg/m³ and viscosity $\hat{\mu}_f$ from 0.058 to 0.373 Pa s (see Table II), where a sphere with diameter of $\hat{D} = 15$ mm and mass density of $\hat{\rho}_p = 1120$ kg/m³ existed. The sphere was initially placed at a height of 120 mm in the fluid at rest, and allowed to fall down by gravitational acceleration of $\hat{a}_g = -9.8$ m/s². The resultant values of the Reynolds number (Re $= \hat{\rho}_f \hat{U}_{max} \hat{D}/\hat{\mu}_f = \hat{U}_{max}\hat{D}/\hat{\nu}_f$) and the

TABLE II. Conditions and results of experiments by ten Cate *et al.* [15] and parameters of our simulations, for a spherical particle sedimenting under gravity in a closed box filled with a fluid.

Case	$\hat{\rho}_f$ (kg/m³)	$\hat{\mu}_f/10^{-3}$ (Pa s)	Re	St	τ	$a_g/10^{-5}$
I	970	373	1.5	0.19	0.80	-8.290
II	965	212	4.1	0.53	0.65	-6.350
III	962	113	11.6	1.50	0.65	-22.21
IV	960	58	32.2	4.17	0.59	-30.22

Stokes number (St $=$ Re $\hat{\rho}_p/9\hat{\rho}_f$) are given in Table II, where $\hat{U}_{max}$ denotes the measured maximum sedimentation speed [15]. In our simulations, the computational domain was divided into $200 \times 200 \times 320$ lattices with $\Delta\hat{x} = 0.5$ mm, the sphere had a diameter of 30 lattices, and the bounce-back condition was applied to all the boundaries of the box. We set the parameters to reproduce the experimental results of Re and St, as given in Table II.

The vertical position and velocity of the sedimenting sphere as a function of time are displayed in Figs. 5(a) and 5(b), respectively, where the experimental results by ten Cate *et al.* [15] are also shown for comparison. For every case, the sedimenting sphere experienced acceleration, steady fall, and deceleration before arriving at the bottom. At smaller Re, the simulation results of SPLBM and iSPLBM were almost
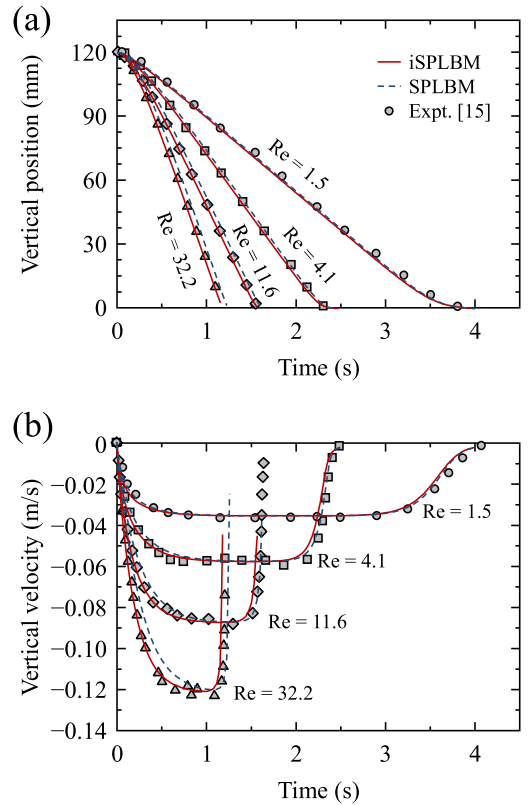

(a)

(b)

FIG. 5. Vertical (a) position and (b) velocity of a sphere sedimenting under gravity in a closed box filled with a fluid as a function of time at different Re. Conditions and parameters of our simulations are summarized in Table II. The results of iSPLBM and SPLBM are compared with experimental results by ten Cate *et al.* [15].

the same and agreed closely with the experimental results during the entire duration. As Re increased, the SPLBM results increasingly deviated from the experimental results; on the other hand, iSPLBM reproduced the sediment motion of the sphere more accurately even for higher Re. These results demonstrate that the forces acting on the solid-side artificial fluid should be considered to obtain accurate simulations of solid particles moving rapidly and with acceleration in a fluid.

D. Flotation of five lightweight spheres

Next, we consider five lightweight spherical particles floating under gravity in a closed box to confirm the stability of our iSPLBM. This phenomenon was simulated by Feng and Michaelides using their IBLBM [17]. Henceforth, the same LBM simulations have been carried out using our iSPLBM. The box had dimensions of $100 \times 100 \times 250$ mm and was filled with fluid of kinematic viscosity, $\hat{v}_f = 0.0002$ m^2/s, where five spheres with diameter of $\hat{D} = 15$ mm existed. The density ratio of particle to fluid was $\hat{\rho}_p / \hat{\rho}_f = 0.8$. Initially, sphere 1 was located at (50, 50, 12.5 mm), and spheres 2–5 were located at (40, 40, 37.5 mm), (60, 40, 37.5 mm), (40, 60, 37.5 mm), and (60, 60, 37.5 mm), respectively, as shown in Fig. 6(a). The computational domain was divided into $80 \times 80 \times 200$ lattices with $\Delta \hat{x} = 1.25$ mm, and the sphere had a diameter of 12 lattices. The relaxation time was $\tau = 0.75$, giving a physical time step of $\Delta \hat{t} = 0.000\,651$ s. The maximal Reynolds number was found to be Re $= \hat{U}_{max} \hat{D} / \hat{v}_f \approx 8$. It is worth noting that a stable simulation of this system was never achieved using conventional SPLBM; however, it was successful using iSPLBM.

Figure 6 shows the snapshots of five floating spheres at $\hat{t} = 0, 0.5$ s, 1.0 s, and 2.5 s. The colors of each sphere represent the vertical velocities of the sphere. Five spheres floated owing to the strong buoyancy force. As shown in Fig. 6(b), the trailing sphere (i.e., sphere 1) rose faster than the leading spheres

(a) $\hat{t} = 0$ (b) 0.5 s   (c) 1.0 s   (d) 2.5 s
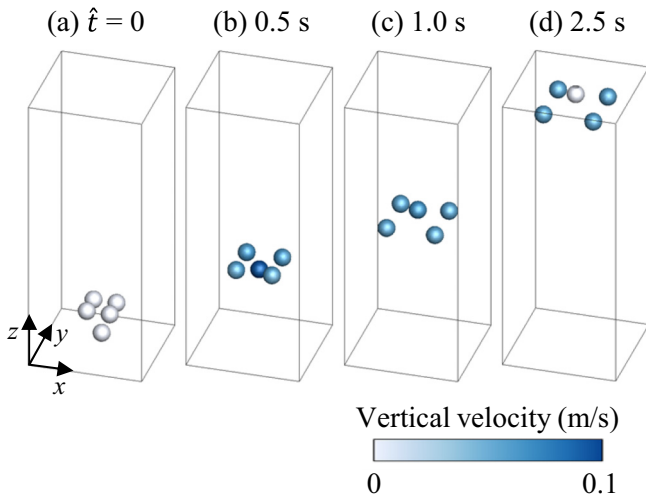

Vertical velocity (m/s)

0   0.1

FIG. 6. Time series snapshots of five spheres floating under gravity in a closed box. The computational conditions and parameters were set to reproduce the simulation by Feng and Michaelides using their immersed-boundary lattice Boltzmann method (IBLBM) [17]. The darker (blue) colors of spheres represent larger vertical velocities.
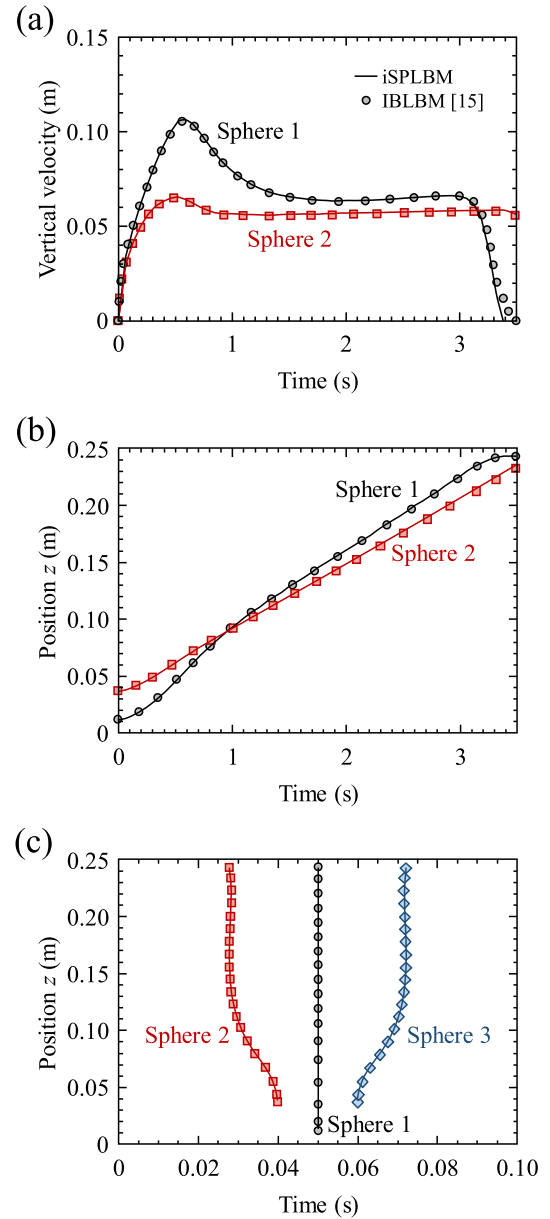

FIG. 7. Vertical (a) velocity and (b) position of spheres 1 and 2 as a function of time, and (c) trajectory of spheres 1–3. The results of iSPLBM are compared with those of the IBLBM simulation by Feng and Michaelides [17].

(i.e., spheres 2–5), because the hydrodynamic resistance force acting on the trailing sphere was reduced by the existence of the leading spheres. Then, the trailing sphere pushed aside the leading spheres to overtake them, as shown in Fig. 6(c). The spheres eventually slowed down before contacting with the top wall, as shown in Fig. 6(d). The vertical velocity and position of spheres 1 and 2 as a function of time are displayed in Figs. 7(a) and 7(b), respectively, and the trajectory of spheres 1–3 is depicted in Fig. 7(c), where the results of the IBLBM simulation by Feng and Michaelides [17] are also shown for comparison. A good agreement between the results of these two simulations demonstrates that our iSPLBM can be stably applied even to the motions of lightweight particles under gravity in a fluid.
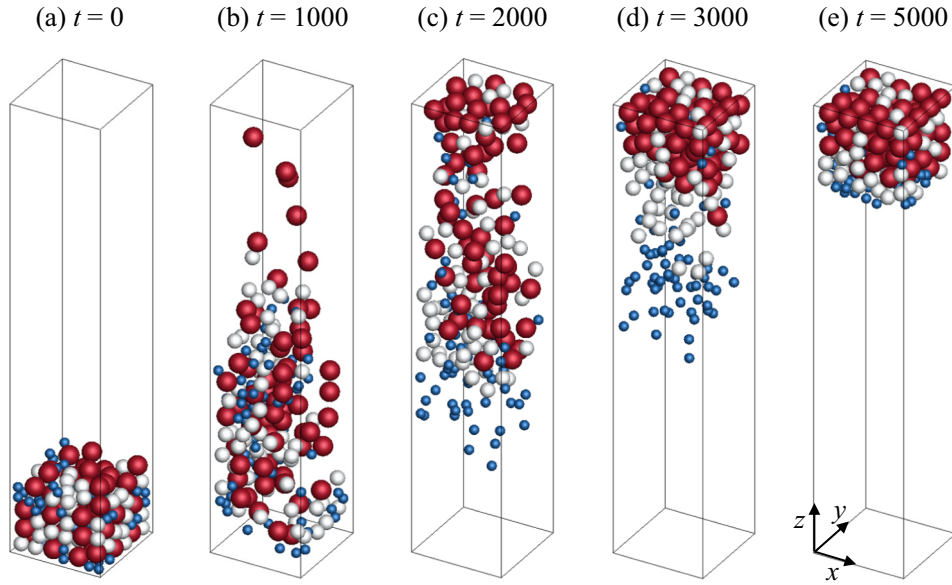
FIG. 8. Time series snapshots of 200 spheres floating under gravity in a closed box filled with a fluid. The spheres had three different diameters of $D = 10\Delta x$ (blue), $15\Delta x$ (white), and $20\Delta x$ (red), and their numbers were set as 72, 65, and 63, respectively.

E. Flotation of 200 lightweight spheres

Finally, we performed a simulation for 200 lightweight spheres floating under gravity. The spheres had a wide range of size distribution. The computational domain had dimensions of $100\Delta x \times 100\Delta x \times 500\Delta x$. The spheres had three different diameters of $D = 10\Delta x$, $15\Delta x$, and $20\Delta x$, and their numbers were set as 72, 65, and 63, respectively. The mass density ratio of sphere to fluid was $\rho_p/\rho_f = 0.9$, the kinematic viscosity of the fluid was $\nu_f = 0.0833$ (i.e., $\tau = 0.75$), and the gravitational acceleration was $a_g = -3.323 \times 10^{-3}$. As shown in Fig. 8(a), 200 spheres with zero velocities were randomly stacked at the bottom of the closed box at time $t = 0$, where the fluid was at rest, and then allowed to float by buoyancy. The maximal Reynolds number defined with mean diameter D_0 was found to be $\mathrm{Re} = U_{max}D_0/\nu_f \approx 10$. In the present study focusing on the hydrodynamic interactions acting on individual spheres and long-distance-range hydrodynamic interactions among the spheres, the direct interactions between the spheres and between the sphere and wall were represented by the repulsive part of the Lennard-Jones potential for the sake of simplicity, although actually they approach to make contact with each other. We should note that the present model can employ in principle more general sphere-sphere and sphere-wall direct interactions such as lubrication force and contact force.

Figure 8 displays a time series of snapshots of 200 floating spheres (these spheres are colored blue, white, and red for $D = 10\Delta x$, $15\Delta x$, and $20\Delta x$, respectively, online). At the initial stage, the spheres with three different sizes were almost completely mixed, as shown in Fig. 8(b). At the middle stage, the floating of smaller spheres tended to be delayed because of the smaller contribution of buoyancy forces, as shown in Figs. 8(c) and 8(d). At the final stage, the spheres were partially segregated according to their sizes near the surface of the

top wall, as shown in Fig. 8(e). Figures 9(a) and 9(b) show the probability distributions of the spheres of three different sizes as a function of the vertical position z at the initial and
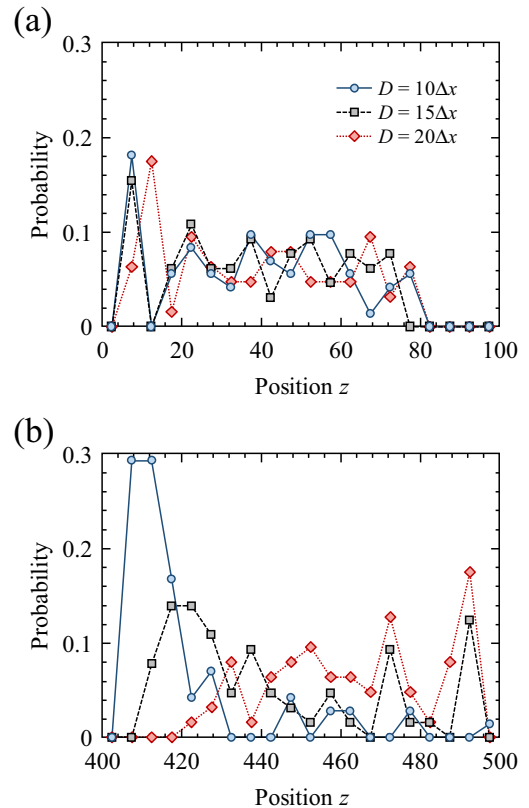

FIG. 9. Probability distribution of spheres of three different sizes as a function of vertical position z at the (a) initial and (b) final states.

final states, respectively. The probability distributions at the initial state were almost homogeneous for every sphere size, whereas a significant segregation according to sphere sizes was observed at the final state. The top particle layer was almost composed of large and medium spheres. The medium spheres were also observed at lower positions, while the existing probability of the large spheres decreased with lower position. On the other hand, the small spheres were clearly segregated at lower positions. This simulation demonstrates that iSPLBM is effective in simulating a large number of floating particles accurately and stably.

Furthermore, it is worth noting that the iSPLBM simulation for spheres of different sizes requires almost the same computation time as that for spheres of equal sizes. This is because the SP method relies only on a fixed Cartesian mesh that is used to calculate the fluid motion as well as the solid-fluid interactions. Therefore, the SP method is fairly suitable for simulation of systems containing many particles with a wide range of size distribution. This advantage is essential in industrial applications, where such particulate flows are frequently encountered and are significantly influenced by the particle size distribution.

V. CONCLUSION

We have developed a computational method for the simulation of particulate flows based on the smoothed-profile (SP) method. In our proposed method, which we call the improved SP (iSP) method, the hydrodynamic force on a moving solid particle is exactly formulated with consideration of the effect of internal fluid mass to improve the accuracy and stability of the smoothed-profile CFD simulations of various particulate flows. In this study, the iSP method is coupled with the lattice Boltzmann method (iSPLBM).

We have carried out numerical simulations of several particulate flow systems and compared our results with those of other simulations and some experiments. Our numerical results have validated the accuracy and stability of iSPLBM. Furthermore, we have performed simulations of flotation of many lightweight particles with a wide range of particle size distribution, which demonstrated the effectiveness of iSPLBM. Finally, it should be noted that our iSP method can also be applied to general DNS solvers. The improved smoothed-profile CFD simulation is an essential tool in understanding and predicting the complicated dynamics of particulate flows.

[1] S. Succi, *The Lattice Boltzmann Equation for Fluid Dynamics and Beyond* (Oxford University Press, Oxford, 2001).

[2] S. Chen and G. D. Doolen, Annu. Rev. Fluid Mech. **30**, 329 (1998).

[3] A. J. C. Ladd, J. Fluid Mech. **271**, 285 (1994).

[4] R. Verberg and A. J. C. Ladd, Phys. Rev. Lett. **84**, 2148 (2000).

[5] P. Lallemand and L. S. Luo, J. Comput. Phys. **184**, 406 (2003).

[6] C. S. Peskin, J. Comput. Phys. **25**, 220 (1977).

[7] Z.-G. Feng and E. E. Michaelides, J. Comput. Phys. **195**, 602 (2004).

[8] Z.-G. Feng and E. E. Michaelides, J. Comput. Phys. **202**, 20 (2005).

[9] J. Wu and C. Shu, J. Comput. Phys. **228**, 1963 (2009).

[10] X. D. Niu, C. Shu, Y. T. Chew, and Y. Peng, Phys. Lett. A **354**, 173 (2006).

[11] Y. Nakayama and R. Yamamoto, Phys. Rev. E **71**, 036707 (2005).

[12] S. Jafari, R. Yamamoto, and M. Rahnama, Phys. Rev. E **83**, 026702 (2011).

[13] M. Fujita and Y. Yamaguchi, J. Comput. Phys. **223**, 108 (2007).

[14] Z. Hashemi, S. Jafari, and M. Rahnama, Comput. Fluids **100**, 65 (2014).

[15] A. ten Cate, C. H. Nieuwstad, J. J. Derksen, and H. E. A. Van den Akker, Phys. Fluids **14**, 4012 (2002).

[16] M. Uhlmann, J. Comput. Phys. **209**, 448 (2005).

[17] Z.-G. Feng and E. E. Michaelides, Comput. Fluids **38**, 370 (2009).

[18] L. Shen, E. S. Chan, and P. Lin, Comput. Fluids **38**, 691 (2009).

[19] K. Suzuki and T. Inamuro, Comput. Fluids **49**, 173 (2011).

[20] T. Inamuro, Fluid Dyn. Res. **44**, 024001 (2012).

[21] X. He and L.-S. Luo, Stat. Phys. **88**, 927 (1997).

[22] S. C. R. Dennis and G. Z. Chang, J. Fluid Mech. **42**, 471 (1970).

[23] H. Dütsch, F. Durst, S. Becker, and H. Lienhart, J. Fluid Mech. **360**, 249 (1998).

[24] C.-C. Liao, Y.-W. Chang, C.-A. Lin, and J. M. McDonough, Comput. Fluids **39**, 152 (2010).